Icarus 396 (2023) 115498

Contents lists available at ScienceDirect

Icarus

journal homepage: www.elsevier.com/locate/icarus

A mid-infrared study of synthetic glass and crystal mixtures analog to the geochemical terranes on mercury

Andreas Morlok [a,*], Christian Renggli [b], Bernard Charlier [c], Olivier Namur [d], Stephan Klemme [b], Maximilian P. Reitze [a], Iris Weber [a], Aleksandra N. Stojic [a], Karin E. Bauch [a], Harald Hiesinger [a], Joern Helbert [e]

[a] Institut für Planetologie, Westfälische Wilhelms-Universität Universität Münster, Wilhelm-Klemm-Straße 10, 48149, Germany
[b] Institut für Mineralogie, Westfälische Wilhelms-Universität Universität Münster, Corrensstrasse 24, 48149 Münster, Germany
[c] University of Liege, Department of Geology, 4000 Sart-Tilman, Belgium
[d] Department of Earth and Environmental Sciences, KU Leuven, 3001 Leuven, Belgium
[e] Institute for Planetary Research, DLR, Rutherfordstrasse 2, 12489 Berlin, Germany

ARTICLE INFO

Keywords:
Mercury, surface
Mineralogy
Infrared observations
Instrumentation
Spectroscopy

ABSTRACT

The MERTIS (MErcury Radiometer and Thermal Infrared Spectrometer) onboard of the BepiColombo ESA/JAXA mission to Mercury will map the surface of Mercury in the wavelength range of 7–14 μm and for the interpretation of these spectra a database of analog materials is needed. We analyzed bulk grain size fractions of a series of analog materials relevant to the distinct terranes of Mercury in diffuse reflectance in the mid-infrared (2.5 μm to 18 μm). Mineral mixtures cover a wide range of modal amounts of forsterite, enstatite, diopside and plagioclase, the resulting spectra can be divided into three distinct groups: (1) is dominated by a single glass feature, (2) by forsterite bands, and (3) by pyroxene bands. Despite often high contents, plagioclase features, are usually 'overprinted' by forsterite and pyroxene bands.

Spectral parameter CF, an easy obtainable proxy for chemistry (SiO_2) and polymerization (SCFM) places the hermean mixtures mostly in the intermediate and basaltic range. The correlation of parameters easily obtainable in remote sensing, Mg/Si ratio, and CF, allows differing materials from high-energy evaporation processes in impacts from such formed in igneous processes.

Preliminary comparison with a spectrum covering most of the hermean surface shows some similarity with band positions of the Inter Crater Plain and Heavily Cratered Terrains (IcP-HCT) and High-Mg Northern Volcanic Plains (High-Mg NVP) mixtures, but none of our spectra is able to reproduce the remote sensing data entirely.

1. Introduction

The mid-infrared spectrometer MERTIS (MErcury Radiometer and Thermal Infrared Spectrometer) of BepiColombo will map the surface of Mercury in the wavelength range of 7–14 μm, with a spatial resolution of around 500 m (Hiesinger et al., 2020). Spectral infrared features permit the direct determination of Mercury's surface mineralogy (e.g., Rothery et al., 2020), which is not possible with ground-based observations at this resolution (e.g., Sprague et al., 2009). In order to extract a more accurate, as well as spatially-resolved mineralogy from the future spectral data, laboratory studies for comparison with BepiColombo measurements are required to support spectral modeling. In order to achieve this, the IRIS (Infrared and Raman for Interplanetary Spectroscopy) laboratory in Münster and the BED (Berlin Emissivity Database) laboratory in Berlin were installed to characterize a wide range of samples relevant to Mercury (e.g. Weber et al., 2018).

There are no known meteorites from Mercury (e.g., Weber et al., 2016). Hence, we rely on remote sensing observations to study the mineralogy of Mercury. Multispectral imaging with the Mercury Dual Imaging System (MDIS) and spectral reflectance measurements with the Mercury Atmospheric and Surface Composition Spectrometer (MASCS) onboard MESSENGER recognized the occurrence of graphite (Peplowski, 2016), sulphides (Vilas, 2016), and ice in polar regions (Neumann, 2013). Spectral measurements also show that the crust of Mercury contains Fe^{2+}-poor silicate minerals (Izenberg et al., 2014). However, spectral data from MESSENGER were insufficient to identify the

* Corresponding author.
E-mail address: morlokan@uni-muenster.de (A. Morlok).

https://doi.org/10.1016/j.icarus.2023.115498
Received 30 November 2022; Received in revised form 14 February 2023; Accepted 23 February 2023
Available online 26 February 2023

mineralogy of silicate phases and their abundances. Additionally, information on the chemical composition of the hermean surface is based on data from X-ray, gamma-ray, and neutron spectrometers onboard the MESSENGER spacecraft (e.g., Peplowski et al., 2011; Peplowski, 2016; Nittler et al., 2020). Major element ratios obtained from the various instruments allowed the identification of several chemically different regions (the so-called 'terranes') on the hermean surface. The terranes were named the Low-Mg Northern Volcanic Plains (Low-Mg NVP), the High-Mg Northern Volcanic Plains (High-Mg NVP), the Smooth Plains, the Inter Crater Plains and Heavily Cratered Terrains (IcP-HCT), and the High-Mg Province (Nittler et al., 2011; Peplowski, 2016; Weider et al., 2015; Vander Kaaden and McCubbin, 2016; Peplowski and Stockstill-Cahill, 2019). Typical rock types on Mercury's surface can broadly be described as Fe-free and S-enriched komatiites, boninites, and andesites (e.g., Weider et al., 2015; Vander Kaaden and McCubbin, 2016; Peplowski and Stockstill-Cahill, 2019). Thermodynamic modeling and experimental petrology provide first order constraints on the mineralogy of such rocks, which are likely to be dominated by olivine, pyroxenes, plagioclase ± quartz, and (Mg,Ca)S sulfide (e.g., Charlier et al., 2013; Stockstill-Cahill et al., 2012; Namur and Charlier, 2017; Vander Kaaden et al., 2017; Renggli et al., 2022). Data from mid-infrared spectroscopy from terrestrial telescopic observations integrating large surface regions also indicate a hermean mineralogy dominated by plagioclase and pyroxene (Donaldson Hanna et al., 2007; Sprague et al., 1994, 2000, 2002, 2007; Sprague and Roush, 1998; Emery et al., 1998; Cooper et al., 2002).

In this study, we performed spectroscopic measurements in the mid-infrared wavelength range of analog glass and crystal mixtures relevant to Mercury's surface. The compositions of the glasses and crystals were chosen based on results from high-temperature crystallization experiments (1480–1100 °C), that were equilibrated at crustal pressure (1 kbar) and reduced redox conditions (around IW-5; Namur and Charlier, 2017). The bulk compositions of these experiments are representative of the five main chemically distinct regions of the hermean surface introduced above, and the quenched products contain some of the following phases: silicate glass, plagioclase, forsterite, diopside, enstatite, quartz, FeSi metal, and sulfide (i.e., stoichiometric FeS). The samples we measured in this study are mixtures of pure endmember minerals and glass, very similar to the chemical compositions of the experimental products presented by Namur and Charlier, 2017. Synthetic glasses used in this study were previously described in detail in Morlok et al. (2021).

The overall aim of this study is to (a) provide mid-infrared reflectance spectra of hermean mineral/glass mixtures in different size fractions to allow granumeletric studies, and under varying observational geometries to accommodate for changing observational conditions in orbit, and (b) provide first spectral parameters for the comparison with future data obtained by MERTIS.

2. Samples and techniques

2.1. Samples

Compositional and mineralogical characteristics of five terranes are covered in this study (Peplowski et al., 2015 and Peplowski and Stockstill-Cahill, 2019, Weider et al., 2015; Namur and Charlier, 2017; Denevi et al., 2020, Nittler et al., 2016). Large lava flows (~3.5 Ga) are typical of the Northern Volcanic Plains (Low-Mg and High-Mg NVP). The Low-Mg NVP is characterized by low Mg/Si ratios and a wider range of Al contents (Weider et al., 2015; Peplowski and Stockstill-Cahill, 2019). This results in high-plagioclase abundance, together with diopside and forsterite, whereas the High-Mg NVP lavas contain higher olivine abundance (Namur and Charlier, 2017).

The intermediate Inter Crater Plain and Heavily Cratered Terrains (IcP-HCT), characterized by medium sized craters, show high Al contents, and contrasting low Mg. This resulted in high modal amounts of plagioclase (Namur and Charlier, 2017; Denevi et al., 2020; Peplowski and Stockstill-Cahill, 2019.)

3.5 to 3.9 Ga old Smooth plains cover ~40% of the hermean surface and are characterized by flat plains with numerous wrinkle ridges. The chemistry shows lower Mg/Si, S/Si, and Ca/Si ratios compared to the other regions, resulting in a mineralogy dominated by plagioclase, but minor mafic components (Weider et al., 2015; Nittler et al., 2011; Namur and Charlier, 2017; Denevi et al., 2020).

The old (4.2–4 Ga) High-Mg Province is characterized by high Mg/Si and Ca/Si, and low Al/Si ratios. The samples used in this study reflect a relatively low abundance series of natural crystalline materials (Table 1) (Namur and Charlier, 2017; Peplowski and Stockstill-Cahill, 2019.) We selected a series of modal (wt%) phase compositions for each surface region identified in Namur and Charlier (2017) (Fig. 1). Chemical bulk compositions of the mixtures were calculated using the chemical composition of the starting materials and the individual weighed phase abundances (Table 2).

Detailed information about the minerals labradorite, enstatite, and forsterite (IDs 28, 53, 249) used in this study are given in Weber et al.

Table 1
Sources of natural crystalline phases used in this study. Samples are from larger, crushed single crystals and handpicked afterwards. Spectra can be found in Fig. 2 f. Chemical data see Table 3.

ID	mineral / features	locality (origin)
13	Quartz	Mongolia
22	Diopside	Otter Lake, Quebec, Canada
28	Labradorite	Ihosy, Madagascar
53	Enstatite	Odegardens Verk, Bamble, Norway
249	Olivine	Dreiser Weiher, Germany

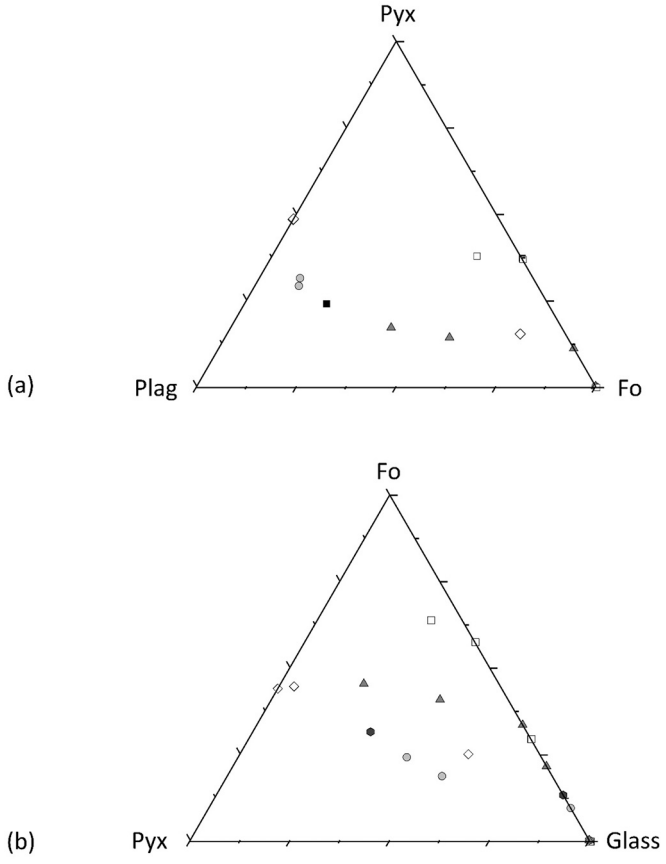

Fig. 1. Overview of the modal composition of the selected samples (Namur and Charlier, 2017). (a) pyroxene, plagioclase, and forsterite, (b) pyroxene, forsterite, and glass. All in wt%.

Table 2
Chemical bulk compositions (wt%) and modal mixtures used in this study. Bulk chemical compositions of the mixtures used in this study (in wt%) were calculated using the chemical compositions of the components and the modal compositions. ID + Number: Sample ID used in the IRIS database (see 2.2. Infrared Studies). Name of sample based on starting composition used following Namur and Charlier (2017). Fo#: Forsterite content, En#: Enstatite content, An#: Anorthite content, Wo#: Wollastonite content (mol.%).

	Low-Mg NVP		High-Mg NVP			Smooth Plains			IcP-HCT			
	ID349 (Y131)_	ID 350 (Y172)_P	ID 355 (Y133)	ID 356 (Y143)	ID 357 (Y144)	ID 345 (Y140)	ID 344 (Y143)	ID 343 (Y144)	ID 351 (Y126)	ID 352 (Y131)	ID 353 (Y132)	ID 354 (Y146)
Glass	86.9	29.5	96.8	42.0	30.2	90.7	53.8	42.3	78.6	66.6	42.3	20.6
Forsterite	8:2	14.3	3.2	12	10.7	9.3	5.1	5.9	21.4	29.7	32.5	31.5
Diopside	4.9	17.1		9.1	12.1		2.2	10.7		3.7	8.1	8.3
Enstatite				16.0	20.3		11.3	7.4				5.0
Plagioclase		39.1		20.8	26.6		27.6	33.7			17.1	33.4
Quartz												1.2
SiO2	64.52	59.35	58.71	59.01	60.41	62.10	61.34	59.76	54,85	59.00	55.73	55.72
TiO2	0.20	0.09	0.40	0.11	0.10	0.42	0.13	0.11	0,28	0.16	0.11	0.07
Al2O3	13.42	15.40	10.61	12.34	12.04	12.97	16.02	15.96	12,98	10.29	11.31	12.47
Cr2O3	0.00	0.01	0.00	0.01	0.01	0.00	0.01	0.01	0,01	0.01	0.02	0.02
FeO	0.97	1.79	0.32	2.80	3.20	0.82	1.63	1.56	1,89	2.70	3.03	3.42
MnO	0.10	0.06	0.17	0.07	0.05	0.16	0.07	0.07	0,08	0.10	0.09	0.06
MgO	9.03	10.57	19.99	14.86	14.68	12.83	9.20	9.22	20,56	18.74	19.78	19.28
CaO	6.25	8.89	6.94	6.91	6.41	6.18	6.53	8.63	5,64	4.79	6.27	5.95
Na2O	5.22	3.92	3.19	3.64	3.29	4.36	4.70	4.34	3,84	4.01	3.46	3.06
K2O	0.20	0.23	0.10	0.17	0.19	0.18	0.21	0.21	0,11	0.16	0.15	0.18
Total	99.91	100.31	100.43	99.93	100.39	100.02	99.85	99.86	100,24	99.97	99.94	100.24
	High-Mg Prov.			Crystalline					Glass			
	ID 348 (Y126)	ID 347 (Y131)	ID 346 (Y146)	ID 249 Forsterite	ID 22 Diopside	ID 53 Enstatite	ID 28 Plagioclase	ID 13 Quarz	ID339	ID 338	ID 181	ID 174
Glass	70.5	42.5	27.7						100	100	100	100
Forsterite	29.5	36.2	35.8	100								
Diopside		21.2	25.3		100							
Enstatite			1.3			100						
Plagioclase			7.7				100					
Quartz			2.0					100				
SiO2	53.87	55.14	56.74	40.96	55.08	57.48	55.63	101.42	58.62	55.90	59.29	64.26
TiO2	0.30	0.11	0.09	0.02	0.05	0.04	0.01	0.01	0.35	0.41	0.41	0.46
Al2O3	7.73	6.63	6.41	0.04	0.31	0.14	27.87	0.01	16.49	7.31	10.95	14.30
Cr2O3	0.01	0.02	0.02	0.04	0.01	0.01	0.02	0.01	0.00	0.00	0.00	0.00
FeO	2.51	3.67	3.90	8.38	2.63	9.09	0.10	0.01	0.13	0.10	0.05	0.05
MnO	0.16	0.11	0.09	0.11	0.14	0.04	0.01	0.01	0.08	0.25	0.17	0.16
MgO	28.30	23.87	23.25	50.50	16.80	33.16	0.01	0.00	12.43	26.94	19.00	8.97
CaO	5.07	7.82	7.71	0.09	25.10	0.21	10.32	0.00	7.15	7.15	7.16	6.81
Na2O	2.33	2.59	2.16	0.01	0.19	0.02	5.29	0.01	4.88	2.95	3.29	4.81
K2O	0.08	0.10	0.13	0.00	0.01	0.01	0.31	0.01	0.14	0.11	0.11	0.19
Total	100.35	100.06	100.51	100.14	100.30	100.21	99.57	101.50	100.27	101.11	100.44	100.01
				Fo#91	En#46Wo#50	En#86	An#51					

(2021), Reitze et al. (2020) and Reitze et al. (2021). ID 22 is a diopside, crushed to grain sizes from 25 μm – 250 μm which shows no sign of impurity. However, in the grain size fraction from 0 μm – 25 μm we observe signs (<5%) of serpentinization (Van der Meer, 1995; Daly et al., 2011). However, this has only small impact on the overall bulk compositions of our samples because we used low proportions of ID 22 Diopside in the mixtures.

The mineral samples are natural terrestrial materials. While the chemical composition of these minerals is, overall, similar to minerals on Mercury, these phases formed in vastly different environments. In particular, terrestrial magmatism is much more oxidized than expected for Mercury, with the latter of which is characterized by redox conditions buffered by the iron-wüstite buffer (IW-7 to IW-3), whereas magmatism on the Earth usually happens at redox conditions between IW-2 to IW + 8 (McCubbin et al., 2012; Namur et al., 2016a, 2016b; Cartier and Wood, 2019). As a result, for example different Fe^{2+}/Fe^{3+} ratios in olivine and pyroxene can be expected. While variations in Fe2+/Fe3+ ratios can affect Si-O-Si bonds and thus potentially affect infrared spectra (e.g. Bingham et al., 2002), a detailed FTIR study by Dufresne et al. (2009) shows no significant effect on band positions and band shapes in the mid-infrared.

Silicate glasses were synthesized to represent the amorphous component in our mixtures.

The glasses were synthesized from oxides, and reduced at the graphite-CO buffer (IW-6.7 at 1450 °C.)

Results were glasses with very low MgO (1.6 wt% - 19.0 wt%), which show features typical for amorphous phases: A strong RB at 9.2 μm and 9.8 μm, and a CF from 7.6 μm to 8.1 μm.

For more details on the synthesis protocol see Morlok et al. (2021).

We produced a series of six synthetic glasses using reagent grade oxides as starting materials. Melts were kept in a gas mixing furnace for 6 h at 1450 °C at the graphite-CO buffer (IW-6.7). The glasses cover the observed compositional range of the terranes (e.g., 1.6 wt% - 19.0 wt% MgO).

Size fractions for each mixture were mixed separately (<25 μm, 25 μm – 63 μm, 63 μm −125 μm, 125 μm −250 μm). This results in minor divergences from the modal starting compositions based on the laboratory experiments (see Table 2). The finest fraction (<25 μm) was chosen to represent the regolith grain size, which exhibits the important Transparency Feature (TF), a characteristic reflectance low. The other size fractions were selected to cover intensity changes related with grain sizes. Increasing grain size is correlated with increasing intensity (e.g., Salisbury, 1993; Mustard and Hays, 1997).

Sample preparation can also have influence on the resulting spectra. Sample preparation induced compressing of samples during preparation can lead to a decrease in porosity. Fine particles start to scatter

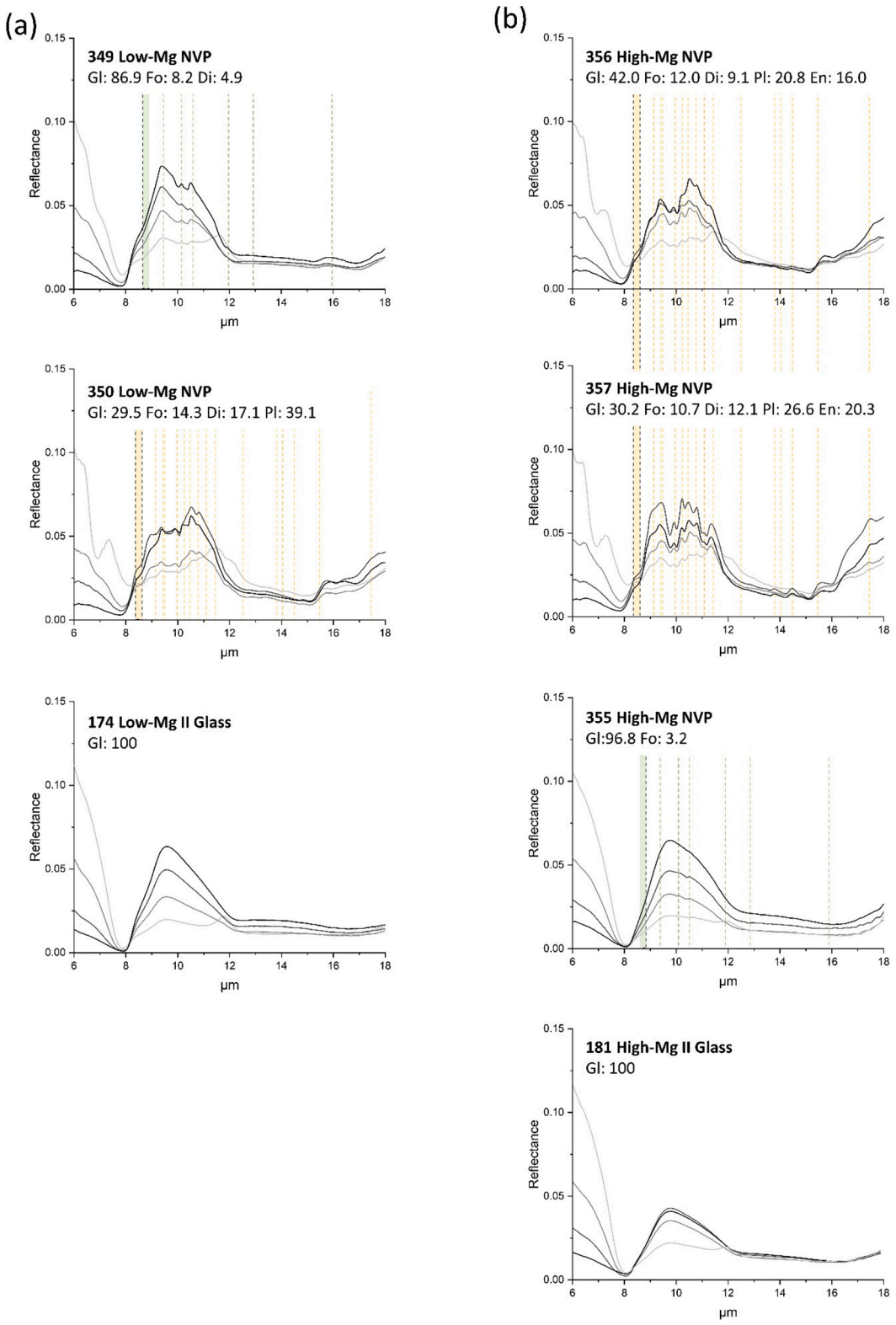

Fig. 2. a-g: Mid-infrared reflectance spectra of the grain size fractions. Black: 125–250 μm, dark grey: 63–125 μm, grey: 25–63 μm, light grey: 0–25 μm. Gl: glass, Fo: forsterite, Di: diopside, Pl: plagioclase, En: enstatite, Qz: quartz. Vertical green lines: 249 forsterite bands, vertical yellow lines: pyroxene features (see Fig. 3). (g) shows wavelength range from 2 to 6 μm covering mainly volatile features.

coherently when they are packed to distances below the wavelength, as result they have the spectral behaviour of larger particles. At larger distances, they act like individual particles and scatter incoherently. So, less porosity of compressed samples increases the surface scattering and thus the intensity of features (Salisbury and Wald, 1992.)

Flattening of the surface can also result in forward scattering,

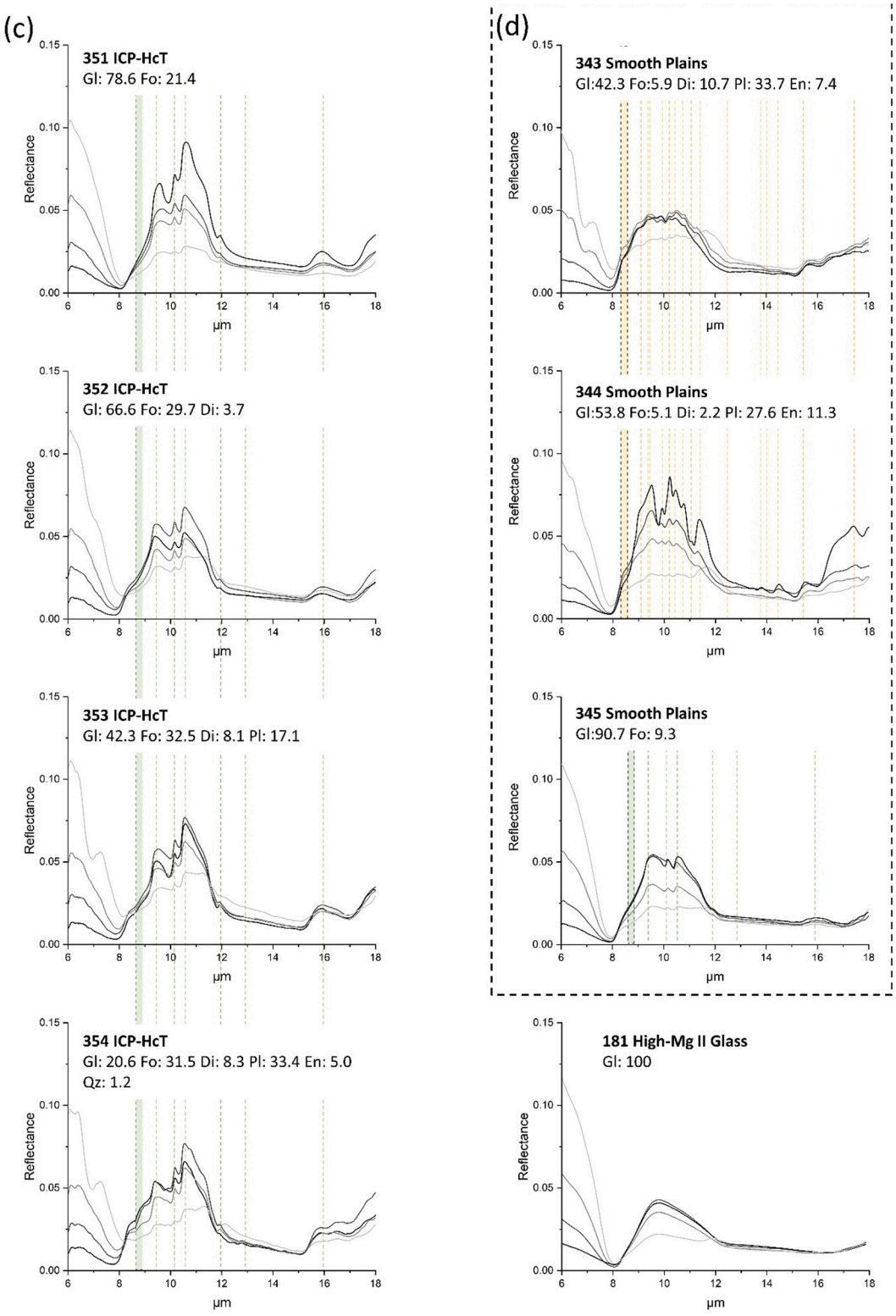

Fig. 2. (*continued*).

affecting relative band intensities (Mustard and Hays, 1997). While it probably is not possible to avoid sample preparation to influence altogether, in order to minimize the effects of sample preparation on the results, a consistent method is necessary that is applied to all samples. In this study, the samples were filled into aluminum sample cups, and the surface flattened with a spatula (see Mustard and Hays, 1997 for details).

2.2. Infrared studies

We used a Bruker Vertex 70v infrared spectrometer with a liquid nitrogen cooled MCT (HgCdTe) detector at the IRIS laboratory in Münster. Analyses were made in the wavelength region of 2.5 μm to 18 μm in low vacuum (100 Pa). For each spectrum, 512 scans were accumulated at a spectral resolution of 4 cm^{-1} (20 nm at 7 μm, 80 nm at 14

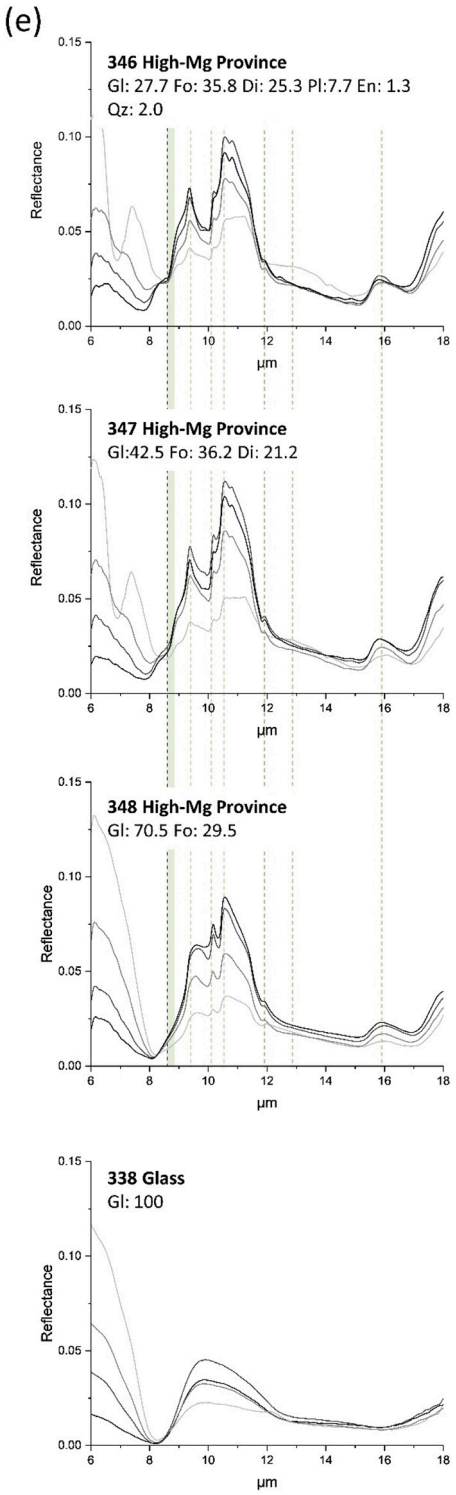

Fig. 2. (*continued*).

μm). This spectral resolution is comparable to MERTIS onboard Bepi-Colombo (e.g., 90 nm, Hiesinger et al., 2010 and 2020). For calibration, the instrument background was eliminated by ratioing the sample spectra against the spectrum of a diffuse gold standard (INFRAGOLD™) measured under the same conditions. Analyses were made at 13° incidence (i) and 13° emergence (e), 20° (i)/30°(e), and 30°(i)/30°(e) in order to simulate observational geometries of an orbiter. The results presented in the main text were made at 20°(i) and 30°(e), results for the other settings are available in the supplement. The results are presented in reflectance from 6 μm – 18 μm (Fig. 2a-e), which covers the range of the MERTIS instrument (7 μm – 14 μm) but omits volatile features. Important features in this range are the Christansen Feature (CF), a reflectance low observable even in spectra with low signal to noise ratio. The CF appears at wavelengths where barely light is scattered owing to an index of refraction near or identical with the surrounding medium (e.g. King et al., 2004).

The CF is also used as proxy for the chemical composition, the feature shifts e.g. with the SiO_2 content (Cooper et al., 2002). The

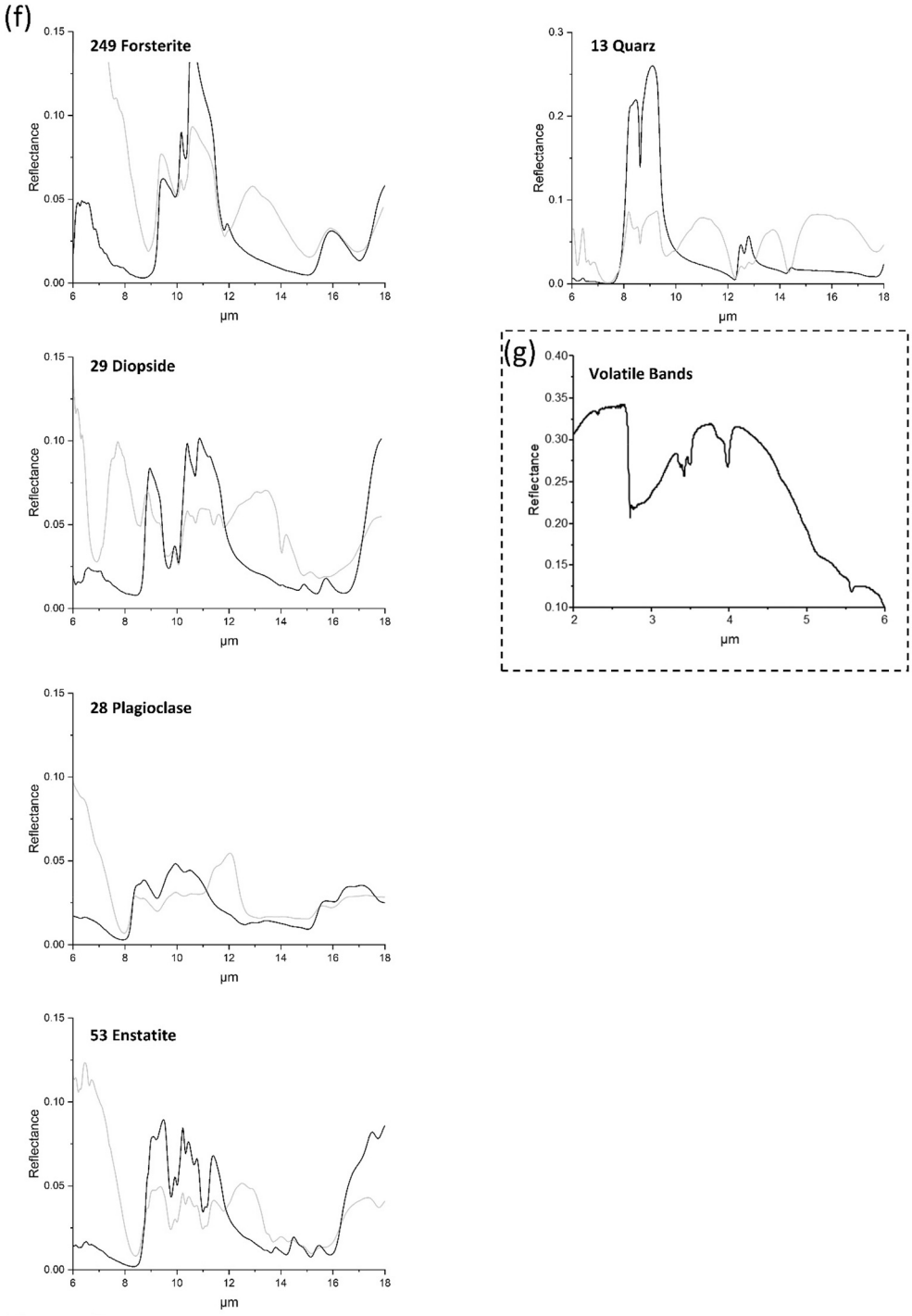

Fig. 2. (*continued*).

Reststrahlenbands (RBs) are the vibration stretching modes of the molecular structure, basically the spectral fingerprint.

Finally, grain size dependent increased volume scattering in spectral ranges of weak absorbance produces the Transparency Feature (TF). The TF appears with decreasing grain size and is strongest for the finest <25 µm size fractions and thus helps determining grain sizes. Band positions of all these features is dependent on the composition of the materials, shifts but also observed with changes in temperature and pressure (Salisbury et al., 1991 and Salisbury et al., 1997.)

Since the aim of our study is to compare the laboratory data with future remote sensing data, measurements from the laboratory have to be recalculated from reflectance to emissivity using Kirchhoff's law: $\varepsilon = 1 - R$ (R = Reflectance, ε = Emission, Nicodemus, 1965). However, a prerequisite for the validity of Kirchhoff's law is that the reflected light should be collected in all directions. In an ideal case directional emissivity and directional hemispherical reflectance should be compared. However, we used a bi-directional setup. Earlier studies showed that this approach mainly affects the reflectance intensity, but not band positions. This must however be kept in mind when comparing the results in a quantitative manner with emission data (Salisbury et al., 1991; Hapke, 1993; Thomson and Salisbury, 1993; Salisbury et al., 1994; Christensen et al., 2001). The spectra presented in this study are accessible on our

online database at the Institut für Planetologie in Münster (http://bc-mertis-pi.uni-muenster.de/).

3. Results

We present the results in the range of interest for silicate features (Fig. 2a-f). However, most samples show spectral features at wavelengths shorter than 7 μm, usually at 2.7 μm – 3.0 μm, 3.4 μm– 4 μm, and 5 μm – 7 μm. These are volatile features due to adsorption of terrestrial water and unavoidable minor contaminations of the terrestrial minerals used for the mixtures (Fig. 2 g).

3.1. Low-mg northern volcanic plains

The glassy end member is represented by low Mg sample ID 174 (Morlok et al., 2021), and has the CF at 7.9 μm, the TF at 11.8 μm, and a single RB at 9.6 μm. The spectrum of ID 350 has the CF between 7.8 μm and 8.1 μm, with several pyroxene RB at 9.4 μm, 9.9 μm, 10.2 μm, 10.5 μm – 10.6 μm and 10.8 μm. The TF is located at 11.3 μm – 11.5 μm (Table 4; Fig. 2a, f). The dominance of the glassy component results in a simpler spectrum with few bands for ID 349: the CF is at 7.8 μm - 7.9 μm, the TF at 11.6 μm. The strongest olivine RB is at 9.4 μm −9.5 μm, with minor features at 10.2 μm and 10.5 μm - 10.6 μm (Table 4; Fig. 2a, f).

3.2. High-mg NVP

The glass-rich samples ID 355 and pure glass ID 181 have the CF at 8 μm to 8.1 μm and the TF at 11.9 μm. They have a strong RB at 9.7 μm to 9.8 μm, ID 355 also has weak olivine bands at 10.5 μm. Crystal-bearing ID 356 and ID 357 show similar pyroxene band positions, although they are different in intensities and band shapes. Their CF is between 7.8 μm and 8.2 μm (Table 4; Fig. 2b, f). Common pyroxene RBs are at 9.4 μm −9.5 μm, 10.2 μm, 10.5 μm, 10.8 μm, and 11.3 μm. At longer wavelengths, bands occur at 14.4 μm–14.5 μm, and 15.6–15.8 μm. The TF is located at 11.4 μm.

3.3. Intra Crater Plains - heavily cratered terrane (IcP-HCT)

The glass endmember, represented by high-Mg glass ID 181 (Morlok et al., 2021) has the CF at 8 μm to 8.1 μm, the TF at 11.9 μm, and a single RB at 9.8 μm. Similar to the High-Mg Province, the spectra of the IcP-HCT region (ID 351, ID 352, ID 353, ID 354) are dominated by olivine features, reflecting the forsterite modes ranging from 21 to 33 wt% (Table 4; Fig. 2c, f). The CF is located between 7.8 μm and 8.2 μm. The strongest RBs are at 9.4 μm - 9.7 μm, 10.2 μm, 10.5 μm–10.6 μm, and 11.9 μm. The TF is again a broad feature without distinct maximum. A dip at 7 μm is observed for diopside-rich samples ID 353 and ID 354.

3.4. Smooth plains

Glass-dominated mixture ID 345 has a CF range from 7.9 to 8 μm, with an RB at 9.6 μm, 10.2 μm and 10.5–10.6 μm. The TF is located at 11.8 μm.

The Smooth Plains samples ID 343 and ID 344 show generally similar pyroxene band positions (Table 4; Fig. 2d, f) reflecting their similar bulk composition, but with ID 344 having more pronounced, 'sharper' bands. The CF is between 7.8 μm and 8 μm for ID 343, and between 7.8 μm and 7.9 μm for ID 344. Significant RBs are between 9.4 μm and 9.6 μm and at 9.9 μm to 10.8 μm and 11.4°μm. The TF is located at 11.7 μm. Various minor spectral features are found at longer wavelengths, mainly from 15.5 μm to 15.8 μm. The diopside-rich sample ID 343 shows a dip at 6.9 μm to 7 μm (or a small feature at 7.3 μm) in the finest grain size fraction.

3.5. High-Mg Province

The glassy end member ID 338 has the CF at 8.2 μm, TF at 12.1 μm and the dominating RB at 9.9 μm

As a result of the high forsterite contents (30–36 wt%), spectra of mixtures ID 346, ID347, and ID348 are quite similar (Table 2; Fig. 2e, f). The plagioclase and pyroxene contents show no significant bands in the spectra. The CF ranges from 7.8 μm to 8.6 μm, and the strongest RB is at 10.6 μm. Further common bands are found at 10.2 μm and 11.9 μm – 12 μm. ID 346 and ID 347 share further RBs at 9.4 μm and 10.8 μm. The TF is a broad feature without a clear peak. Features at longer wavelengths are seen between 15.8 μm and 16 μm. Samples ID 346 and ID 347 shows a dip at 6.9 μm in the finest grain size fractions.

Table 3
Overview of the groups into which the mixture spectra can be divided based on their dominant features.

	RB Features	Samples
ID 338, 181,174 Glass	9.6–9.9 μm	ID 174, ID181, ID 338, ID 355 High-Mg NVP
ID 249 Forsterite	9.4 μm- 9.5 μm, 10.2 μm, 10.6 μm, 11.9 μm, 15.9 μm −16 μm	ID 349 Low-Mg NVP, ID 346, 347, 348 High-Mg Prov., ID 351, 352,353, 354 IcP-HCT, ID 345 Smooth Plains, ID 355 High-Mg NVP
ID53 Enstatite/ 29 Diopside	8.9 μm - 9.1 μm, 9.4 μm - 9.5 μm, 9.9 μm, 10.2 μm, 10.4 μm–10.8 μm, 11 μm–11.1 μm - 11.3 μm, 11.4 μm to 11.6 μm	ID 350 Low-Mg NVP, ID 343, 344 Smooth Plains, ID 356, 357 High-Mg NVP

4. Discussion

4.1. Interpreting the mixtures

Despite the often-complex mixtures of up to five crystalline and one amorphous phase, the resulting spectra of the mixtures can be divided into three groups (Table 3). The simplest spectra are dominated by glass, demonstrated by prominent RB from 7.9 μm – 8.3 μm. Besides the 'pure' glassy end members (ID 174, ID181, and ID 338), sample ID 355 High-Mg NVP with only minor (3 wt%) crystalline content shows barely any recognizable additional bands (Fig. 2b). In the second group, forsterite features tend to dominate (Table 3): bands near 9.4 μm to 9.5 μm, 10.2 μm, 10.6 μm, 11.9 μm, and 15.9 μm −16 μm (Fig. 2c, e). In the finest size fraction (< 25 μm), the TF is turned into a broader feature with another peak at 11.2 μm to 11.3 μm.

A third group exhibits the pyroxene RB features of diopside and enstatite near 8.9 μm to 9.1 μm, 9.4 μm - 9.5 μm, 9.9 μm, 10.2 μm, 10.4 μm - 10.8 μm, 11 μm - 11.1 μm - 11.3 μm, and 11.4 μm to 11.6 μm (Fig. 2a-e). The finest grain size fractions of diopside-rich samples also show a dip at 6.9 μm to 7 μm, which is also prominent in the finest grain size fraction of the ID 22 diopside bulk material.

Although plagioclase feldspar is often a dominant component in the mixtures, its RB features tend to be subdued by the forsterite and enstatite bands. The only RB, which is visible in all samples with a high amount of plagioclase is its RB 1 as a shoulder at around 8.3 μm (e.g. 356 and 357 High-Mg NVP; Fig. 4b). This is probably caused by its flat spectrum, that is dominated by a broad RB at 8.7 μm, and particular at 9.9 μm to 10 μm and 10.5 μm to 10.6 μm, which are superimposed by the more pronounced pyroxene and olivine bands. However, further hints of significant plagioclase contents are higher intensities in the ⁓10 μm to 10.5 μm range due to the strong plagioclase double-feature, which provides a generally broad feature, which serves as some kind of

Table 4
Band positions of the studied mixtures. In Bold: position of the CF of the respective grain size fractions. (In μm).

Smooth Plains	CF													
ID 343														
0–25 μm	8.04	9.01	9.63	9.92	10.20	10.54	10.82			11.65			15.69	
25–63 μm	7.93		9.51	9.92	10.23	10.49	10.78		11.27				15.77	
63–125 μm	7.90		9.40	9.91	10.23	10.49	10.78						15.76	
125–250 μm	7.84		9.62	9.89	10.21	10.46							15.69	
ID 344														
0–25 μm	7.91		9.54	9.87	10.18	10.51				11.67		14.43		
25–63 μm	7.89		9.53	9.90	10.18	10.48			11.28		13.75	14.43	15.69	
63–125 μm	7.84		9.51	9.89	10.20	10.48			11.30			14.47	15.65	
125–250 μm	7.83		9.51	9.91	10.22	10.45	10.76	11.06	11.38		13.79	14.47	15.53	
ID 345														
0–25 μm	7.97		9.59		10.16	10.56			11.42	11.75			15.81	16.01
25–63 μm	7.93		9.58		10.17	10.55							15.85	16.08
63–125 μm	7.91		9.61		10.16	10.50							15.78	15.96
125–250 μm	7.89		9.59		10.17	10.56								15.93
ID 174														
0–25 μm	7.89		9.58							11.78				
25–63 μm	7.87		9.58											
63–125 μm	7.91		9.58											
125–250 μm	7.91		9.58											
High-Mg Province														
ID 346														
0–25 μm	8.60		9.37		10.19	10.64						14.12	16.03	
25–63 μm	7.91		9.37		10.19	10.57	10.79		11.21	11.92		14.84	15.93	
63–125 μm	7.81		9.36		10.19	10.56	10.80			11.90		14.85	15.83	
125–250 μm	7.77		9.36			10.55	10.81			12.41		14.86	15.80	
ID 347														
0–25 μm	8.53		9.39		10.18	10.64	10.84					14.10	16.08	
25–63 μm	8.03		9.38		10.19	10.57	10.79			11.90			15.91	
63–125 μm	7.87		9.38		10.18	10.57	10.79			11.92			15.81	
125–250 μm	7.83		9.37		10.18	10.56	10.79			11.92			15.81	
ID 348														
0–25 μm	8.21		9.63		10.16	10.64				11.96			15.96	
25–63 μm	8.14		9.56		10.16	10.59				11.92			15.94	
63–125 μm	8.11		9.66		10.18	10.57				11.89			15.98	
125–250 μm	8.08		9.61		10.17	10.56				11.89			15.89	
ID 338														
0–25 μm	8.27			9.90						12.06				
25–63 μm	8.21			9.84										
63–125 μm	8.22			9.90										
125–250 μm	8.20			9.87										

Low-Mg NVP	**CF**												
ID 349													
0–25 μm	**7.88**			9.45		10.16	10.56				11.62	15.66	
25–63 μm	**7.85**			9.40		10.16	10.52					15.79	
63–125 μm	**7.80**			9.39		10.16	10.48					15.71	
125–250 μm	**7.76**			9.39		10.15	10.50					15.82	
ID 350													
0–25 μm	**8.14**	8.36		9.40	9.89		10.62			11.32	11.50	15.73	
25–63 μm	**7.86**			9.36	9.89		10.52	10.82				15.77	
63–125 μm	**7.82**			9.36	9.91		10.52	10.81				15.77	
125–250 μm	**7.76**			9.39	9.89	10.19	10.52					15.93	
ID 174													
0–25 μm	**7.89**			9.58							11.78		
25–63 μm	**7.87**			9.58									
63–125 μm	**7.91**			9.58									
125–250 μm	**7.91**			9.58									
IcP-HCT													
ID 351													
0–25 μm	**8.15**			9.63		10.15	10.61				11.94	16.12	
25–63 μm	**8.09**			9.62		10.15	10.55				11.91	15.95	
63–125 μm	**8.04**			9.68		10.16	10.55					15.95	
125–250 μm	**8.02**			9.57		10.16	10.59				11.92	15.91	
ID 352													
0–25 μm	**8.14**			9.54		10.16	10.64			11.30	11.90	15.92	
25–63 μm	**7.87**			9.48		10.16	10.58					15.91	
63–125 μm	**7.83**			9.44		10.16	10.55				11.91	15.91	
125–250 μm	**7.79**			9.39		10.16	10.55				11.90	15.91	
ID 353													
0–25 μm	**8.15**			9.66		10.16	10.62			11.24	11.92	16.01	
25–63 μm	**7.98**			9.52		10.18	10.57				11.90	15.90	

(*continued on next page*)

Table 4 (*continued*)

Low-Mg NVP	CF											
63–125 μm	**7.86**		9.53		10.18	10.57			11.90	15.94		
125–250 μm	**7.80**		9.46		10.16	10.57			11.93	15.90		
ID 354												
0–25 μm	**8.18**	8.34	9.46	9.93	10.18	10.72			12.14	16.01	16.47	
25–63 μm	**7.89**		9.48		10.18	10.56			11.92	15.96	16.35	
63–125 μm	**7.85**		9.39	9.91	10.18	10.54			11.91	15.88	16.49	
125–250 μm	**7.75**		9.39		10.18	10.55				15.88	16.48	
ID 181												
0–25 μm	**8.08**			9.80					11.91			
25–63 μm	**8.07**			9.80								
63–125 μm	**8.06**			9.78								
125–250 μm	**8.04**			9.81								

High-Mg NVP	CF											
ID 355												
0–25 μm	**8.08**			9.83		10.48		11.86				
25–63 μm	**8.06**			9.74		10.50						
63–125 μm	**8.04**			9.79		10.50						
125–250 μm	**8.05**			9.79								
ID 356												
0–25 μm	**8.08**		9.42	9.89	10.23	10.51	10.79	11.43		14.42		
25–63 μm	**7.96**		9.48	9.89	10.20	10.51		11.30		14.43	15.74	
63–125 μm	**7.87**		9.42	9.89	10.24	10.49				14.42	15.78	
125–250 μm	**7.86**		9.39	9.89		10.51	10.79			14.42	15.74	
ID 357												
0–25 μm	**8.15**	8.38	9.39	9.90	10.23	10.52	10.79	11.44		14.41	15.73	
25–63 μm	**7.89**		9.42	9.91	10.21	10.53	10.77	11.33		14.42		17.46
63–125 μm	**7.83**		9.40	9.91	10.22	10.46	10.79	11.34	13.77	14.48	15.63	17.51
125–250 μm	**7.81**		9.37	9.91	10.21	10.49	10.79	11.34	13.77	14.48	15.70	17.54
ID 181												
0–25 μm	**8.08**			9.80				11.91				
25–63 μm	**8.07**			9.80								
63–125 μm	**8.06**			9.78								
125–250 μm	**8.04**			9.81								

underlying continuum, as observed in samples ID 350 and ID 356 (Fig. 2a, b). In the wavelength range around 12 μm glasses and plagioclases have overlapping TF. In earlier experiments using plagioclase (ID28) with varying degrees of Al—Si order (Reitze et al., 2021) plagioclases with low degree of Al—Si order show a single TF, such with a higher order a double peak or peak with shoulder, as seen in the case of the plagioclase ID28 used in this study (e.g. 350 Low-Mg NVP or 357 High-Mg NVP; Fig. 2a, b).

The quartz content is too low (few wt%) to produce any recognizable RB (e.g., 2 wt% in ID 346, 1.2 wt% in ID 354; Fig. 4b and e). This raises the question of the 'critical' concentration (i.e. detection limit) of a phase to be recognizable in a mixture. In simple mixtures of glass and a crystalline phase, minute contents of 3 wt% olivine in ID 355 High-Mg NVP(Fig. 2b) provide just enough signal to identify the mineral with features at 10.5 μm and 11.9 μm (Table 4). Contents of 9.3 wt% olivine in ID 345 Smooth Plains (Fig. 2d) are easily recognizable with bands at 9.6 μm, 10.2 μm, 10.6 μm, and 11.4 μm (Table 4). However, two minor components of 8.2 wt% olivine and 4.2 wt% diopside in ID 349 Low-Mg NVP (Fig. 4a) only allow the clear identification of the olivine 9.4–9.5 μm, 10.2 μm, 10.5 μm–10.6 μm, and 11.6 μm. Increasing number of phases will make the identification of a minute phase in the crowded range around 10 μm difficult. For the semi-quantitative identification of further components, rationing of spectral parameters could provide an alternative.

4.2. Correlation of bulk composition with spectral parameters

4.2.1. Christiansen feature and SiO_2

The CF can be extracted even from 'noisy' spectra. Hence any correlation of the CF with other features will help to derive basic information about composition and mineralogy from remote sensing data. A classical method to correlate the average CF of all grain size fractions with chemical composition is the comparison of the SiO_2 content (wt%) with the CF (Cooper et al., 2002). The comparison of the hermean mixtures in this study with earlier results (Fig. 3a) (Morlok et al., 2016a, 2016b, 2017, 2020a, 2020b; Morlok et al., 2021) shows that most of the mixtures fall close to the correlation line for terrestrial materials, which is the best fit for results of a range of terrestrial rocks scattering a bit due to compositional variances as indicated by the blue shaded areas (Cooper et al., 2002). Furthermore, the results fall into or very close to the field for intermediate rocks.

4.2.2. Christiansen feature and bulk Mg/Si

Absolute element abundances are difficult to determine from mid-IR remote sensing data. Hence, we use the element ratio between Mg and Si for a correlation with the CF, as ratios of chemical data of two major elements is easier to extract from the space probe data (Fig. 3b). In combination with the CF it provides a set of parameters relatively easily extracted from remote sensing data.

Here, our results fall along the area of synthetic Mercury composition glasses (Morlok et al., 2017; Morlok et al., 2020a). The terrestrial impact glasses and the refractory glass from laser-heated melting experiments (Morlok et al., 2020b) are clearly in a separate field compared to our samples relevant to Mercury. This separation could help to identify glassy material formed in high-velocity impacts from such produced in volcanic processes.

4.2.3. Christiansen feature and SCFM

The SCFM index expresses the degree of polymerization based on the $SiO_2/SiO_2 + CaO + FeO + MgO$ relation (Salisbury and Walter, 1989). Similar to earlier studies, most of the results plot systematically below the terrestrial correlation line (Fig. 4c). This could be related to the varying degrees of polymerization of the mixtures, however the correlation between glass content and SCFM is very weak ($R^2 = 0.04$) The

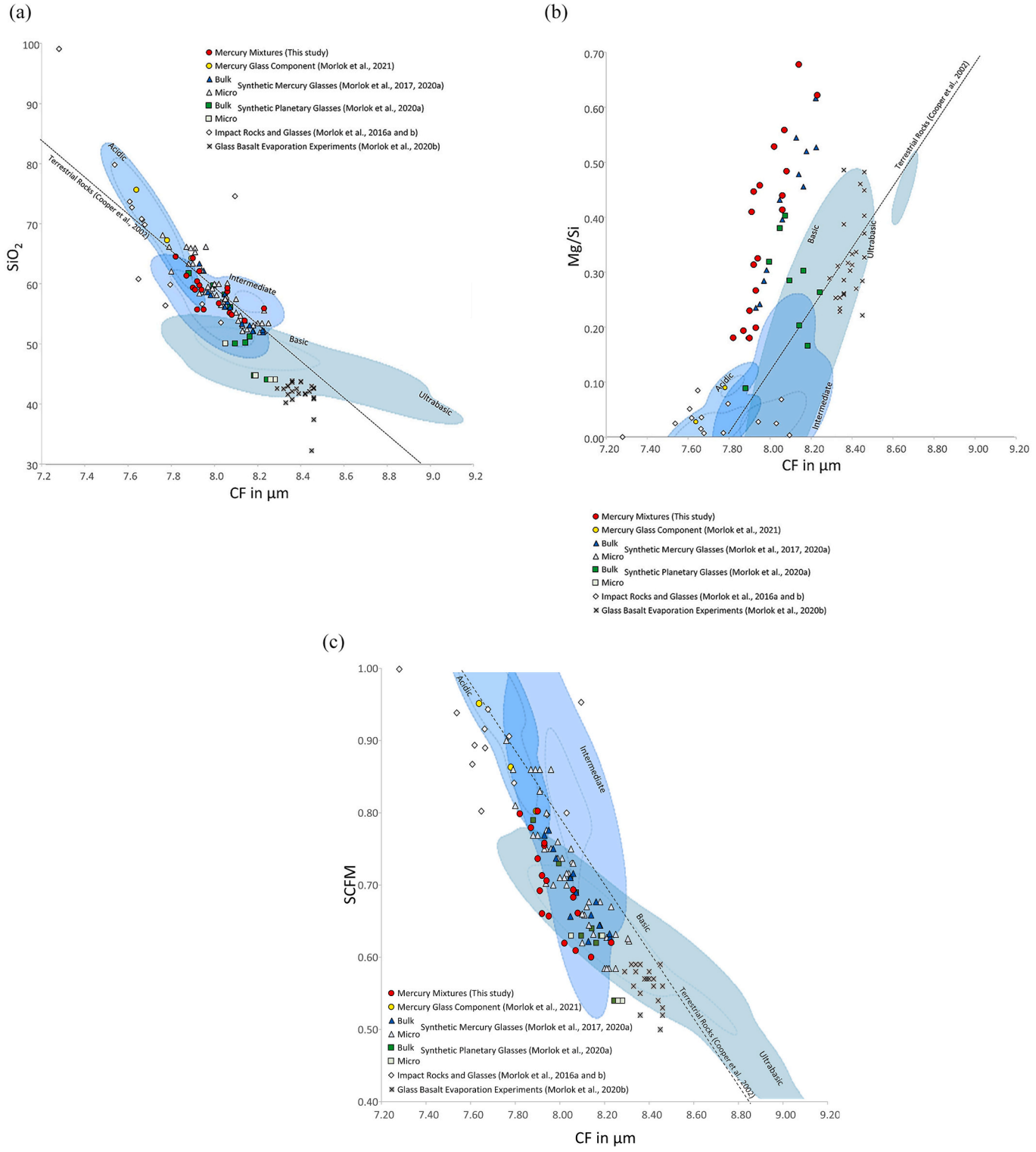

Fig. 3. (a) Correlation of SiO_2 abundance with CF position. Results from this study (red circles) mainly fall into the intermediate area. (b) Comparison of the Mg/Si ratio with the CF. The refractory glasses produced with laser-heating (Morlok et al., 2020b) is easy to distinguish from the samples with hermean and planetary compositions. (c) Comparison of SCFM (SiO_2, CaO, FeO, MgO) index of polymerization to CF position. Blue shaded areas and dashed line mark are from Cooper et al. (2002) for terrestrial rocks. (For interpretation of the references to colour in this figure legend, the reader is referred to the web version of this article.)

results show similarities to the intermediate, basic and basaltic terrestrial rocks (Cooper et al., 2002).

4.3. Comparison with remote sensing data of mercury

Only few mid-infrared spectra are so far available for Mercury. Owing to technical reasons they cover larger surface regions (10^4–10^6 km^2) and offer only weak spectral contrast and low signal to noise ratios

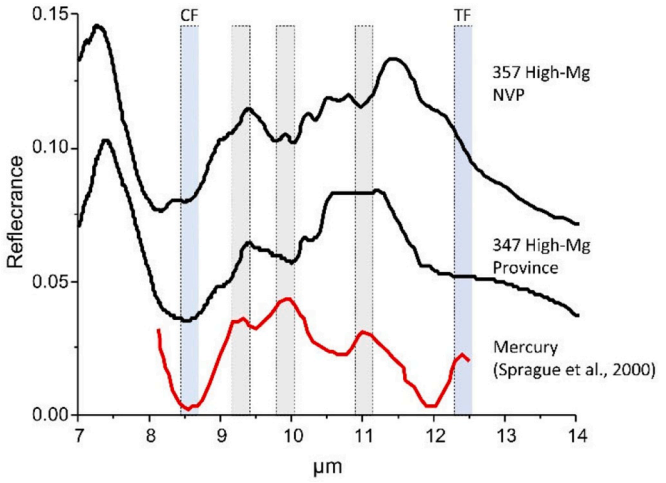

Fig. 4. Comparison of Plagioclase and enstatite-rich 357 High-Mg NVP, and olivine-rich 347 High-Mg Province mixtures with a Mercury surface spectrum (recalculated from emissivity) (Sprague et al., 2000, 2007). Shaded areas mark characteristic features of the hermean spectrum.

(Sprague et al., 2007). Therefore, we only use as an example the spectrum with the highest signal to noise for our comparisons. The spectrum integrates a region at about 210–250° longitude and was obtained by the Mid Infrared Camera (MIRAC) at the Kitty Peak Observatory (Sprague et al., 2000).

The spectrum recalculated from emission (Fig. 4) shows a CF at 8.5 μm, three strong RBs at 9.3°μm, 9.9°μm, and 11°μm. A potential TF is visible at 12.4°μm. We compare it with our results of the 0–25 μm fraction of two mixtures reproducing some of the features.

The olivine-rich 347 High-Mg Province mixture reproduces the CF of the hermean spectrum, and also has an RB at 9.4 μm, near the 9.3 μm feature of the surface spectrum. A broad feature at 11°μm overlaps with a (much narrower) band of the surface spectrum at the same position.

Plagioclase and enstatite-rich 357 High-Mg NVP mixture has a low-point at 8.5 μm, a strong RB at 9.4°μm and a minor RB at 9.9°μm. These features are similar to the CF at 8.5 μm and the second and third RB (9.3°μm and 9.9°μm) of the hermean sample.

However, for a detailed comparison of laboratory spectra to remote sensing data of the hermean surface, the different environment – heat and high vacuum – have to be considered. Both factors affect band intensities as well as positions (e.g. Donaldson Hanna et al., 2007). The impact of these factors will be investigated in upcoming studies.

5. Summary & conclusions

We mixed bulk grain size fractions of analog materials relevant to the distinct terranes of Mercury. The powdered samples were analyzed in diffuse reflectance in the mid-infrared (2 μm – 20 μm).

The resulting spectra can be divided into three groups: (1) such as dominated by a single glass feature, (2) a group with forsterite, and (3) a group dominated by pyroxene bands. Plagioclase features, even when the phase is dominating the composition, are usually 'overprinted' by forsterite and pyroxene bands.

The spectral parameter CF in comparison with chemistry (SiO_2) and polymerization (SCFM) places the hermean mixtures mostly in the intermediate and basaltic range, similar to findings based in Peplowski and Stockstill-Cahill (2019). The correlation of parameters Mg/Si ratio and CF, that are easily obtainable in remote sensing, allows to distinguish materials that were formed by high energy evaporation processes in impacts from those formed by melting processes.

Preliminary comparison with a high-quality spectrum of the hermean surface (Sprague et al., 2000) show some similarity with band positions of IcP-HCT and High-Mg NVP mixtures, but none of our spectra is able to reproduce the remote sensing data entirely.

This is not unexpected since further conditions (e.g. temperature) will also affect spectral properties, and this will have to be addressed by future studies. Furthermore, the materials produced for this study will be used in a follow-up study of Space Weathering effects.

Declaration of Competing Interest

None.

Data availability

Data will be made available on request.

Acknowledgements

A.M., M.P.R., A.N.S., I.W. and H.H. are supported by the DLR grant 50QW1701 and 50QW2201A1302. CR is funded by the Deutsche Forschungsgemeinschaft (DFG, German Research Foundation) – project 442083018. BC is a Research Associate of the Belgian Fund for Scientific Research-FNRS. ON acknowledges support from the FWO through an Odysseus grant.

References

Bingham, P.A., Parker, J.M., Searle, T., Williams, J.M., Smith, I., 2002. Novel structural behaviour of iron in alkali-alkaline-earth-silica glasses. Comptes Rendus Chimie 5, 787–796.
Cartier, C., Wood, B.J., 2019. The role of reducing conditions in building mercury. Elements 15, 39–45.
Charlier, B., Grove, T.L., Zuber, M.T., 2013. Phase equilibria of ultramafic compositions on mercury and the origin of the compositional dichotomy. Earth Planet. Sci. Lett. 363, 50–60.
Christensen, P.R., Bandfield, J.L., Hamilton, V.E., 2001. Mars global surveyor thermal emission spectrometer experiment: investigation description and surface science results. J. Geophys. Res. 106 (ElO), 23823–23872.
Cooper, B.L., Salisbury, J.W., Killen, R.M., Potter, A.E., 2002. Midinfrared spectral features of rocks and their powders. J. Geophys. Res. 107 (E4), 5015–5017.
Daly, T., Gavin, P., Chevrier, V., 2011. Effects of thermal alteration on the near-infrared and mid-infrared spectra of martian phyllosilicates. In: 42nd Lunar and Planetary Science Conference, LPI Contribution No. 1608, p. 1164.
Denevi, B.W., Ernst, C.M., Prockter, L.M., Robinson, M.S., 2020. The geologic history of mercury. In: Salomon, Nittler, Anderson (Eds.), Mercury – The View after Messenger. Cambridge.
Donaldson Hanna, K.L., Greenhagen, B.T., Patterson, W.R., Pieters, C.M., Mustard, J.F., Bowles, N.E., Paige, D.A., Glotch, T.D., Thompson, C., Emery, J.P., Sprague, A.L., Witteborn, F.C., Colwell, F.C., 2007. Effects of varying environmental conditions on emissivity spectra of bulk lunar soils: Application to Diviner thermal infrared observations of the Moon. Icarus 283, 326–342.
Dufresne, C.D.M., King, P.L., Dyar, D., et al., 2009. Effect of Si02, total FeO, Fe3+ /Fe2+, and alkali elements in basaltic glasses on mid-Infrared spectra. Am. Mineral. 94, 1580–1590.
Emery, J.P., Sprague, A.L., Witteborn, F.C., Colwell, J.E., Kozlowski, R.W.H., Wooden, D. H., 1998. Mercury: thermal Modeling and Mid-infrared (5-12 μm) Observations. Icarus 136, 104–123.
Hapke, B., 1993. Theory of Reflectance and Emittance Spectroscopy. Cambridge Univ, Press, New York.
Hiesinger, H., Helbert, J., Mertis Co-I Team, 2010. The Mercury Radiometer and Thermal Infrared Spectrometer (MERTIS) for the BepiColombo mission. Planet. Space Sci. 58, 144–165.
Hiesinger, H., Helbert, J., Alemanno, G., Bauch, K.E., D'Amore, M., Maturilli, A., Morlok, A., Reitze, M.P., Stangarone, C., Stojic, A.N., Varatharajan, I., Weber, I., the MC-IT, 2020. Studying the composition and mineralogy of the hermean surface with the mercury radiometer and thermal infrared spectrometer (MERTIS) for the BepiColombo Mission: an update. Space Sci. Rev. 216 (6), 110. https://doi.org/10.1007/s11214-020-00732-4.
Izenberg, N.R., et al., 2014. The low-iron, reduced surface of Mercury as seen in spectral reflectance by MESSENGER. Icarus 228, 364–374.
King, P.I., McMillan, P.F., Moore, G.M., 2004. Infrared spectroscopy of silicate glasses with application to natural systems. In: King, P.L., Ramsey, M.S., Swayze, G.A. (Eds.), Infrared Spectroscopy in Geochemistry, Exploration Geochemistry, and Remote Sensing, Mineral, Assoc. of Can. Short Course Ser, 33. Mineralogical Association of Canada, Ottawa, pp. 93–133.
McCubbin, F.M., Riner, M.A., Vander Kaaden, K.E., Burkemper, L.K., 2012. Is Mercury a volatile-rich planet? Geophys. Res. Lett. 39, L09202. https://doi.org/10.1029/2012GL051711.

Morlok, A., Stojic, A., Dittmar, I., Hiesinger, H., Tiedeken, M., Sohn, M., Weber, I., Helbert, J., 2016a. Mid-infrared spectroscopy of impactites from the Nördlinger Ries impact crater. Icarus 264, 352–368.
Morlok, A., Stojic, A., Weber, I., Hiesinger, H., Zanetti, M., Helbert, J., 2016b. Mid-infrared bi-directional reflectance spectroscopy of impact melt glasses and tektites. Icarus 278, 162–179.
Morlok, A., Klemme, S., Weber, I., Stojic, A., Sohn, M., Hiesinger, H., 2017. IR spectroscopy of synthetic glasses with mercury surface composition: analogs for remote sensing. Icarus 296, 123–138.
Morlok, A., Klemme, S., Iris, Weber, Stojic, A., Sohn, M., Hiesinger, H., Helbert, J., 2020a. Mid-infrared spectroscopy of planetary analogs: A database for planetary remote sensing. Icarus 324, 86–103.
Morlok, A., Hamann, C., Martin, D., Weber, I., Joy, K.H., Hiesinger, H., Wogelius, R., Stojic, A.N., Helbert, J., 2020b. Mid-infrared spectroscopy of laser-produced basalt melts for remote sensing application. Icarus 335, 113410.
Morlok, A., Renggli, C., Charlier, B., Reitze, M.P., Klemme, S., Namur, O., Sohn, M., Martin, D., Weber, I., Stojic, A.N., Hiesinger, H., Joy, K.H., Wogelius, R., Tollan, P., Carli, C., Bauch, K.E., Helbert, J., 2021. Mid-infrared reflectance spectroscopy of synthetic glass analogs for Mercury surface studies. Icarus 361, 114363.
Mustard, J.F., Hays, J.E., 1997. Effects of hyperfine particles on reflectance spectra from 0.3 to 25 μm. Icarus 125, 145–163.
Namur, O., Charlier, B., 2017. Silicate mineralogy at the surface of mercury. Nat. Geosci. 10, 9–13.
Namur, O., Collinet, M., Charlier, B., Grove, T.L., Holtz, F., McCammon, C., 2016a. Melting processes and mantle sources of lavas on Mercury. Earth Planet. Sci. Lett. 439, 117–128.
Namur, O., Charlier, B., Holtz, F., Cartier, C., McCammon, C., 2016b. Sulfur solubility in reduced mafic silicate melts: Implications for the speciation and distribution of sulfur on Mercury. Earth Planet. Sci. Lett. 448, 102–111.
Neumann, G.A., 2013. Bright and dark polar deposits on Mercury: Evidence for surface volatiles. Science 339, 296–300.
Nicodemus, F.E., 1965. Directional reflectance and emissivity of an opaque surface. Appl. Opt. 4, 767.
Nittler, L.R., Starr, R.D., Weider, S.Z., McCoy, T.J., Boynton, W.V., Ebel, D.S., Ernst, C.M., Evans, L.G., Goldsten, J.O., Hamara, D.K., 2011. The major-element composition of Mercury's surface from MESSENGER X-ray spectrometry. Science 333, 1847–1849.
Nittler, L.R., Frank, E.A., Weider, S.Z., Crapster-Pregont, E., Vorburger, A., Starr, R.D., Solomon, S.C., 2020. Global major-element maps of Mercury from four years of MESSENGER X-Ray Spectrometer observations. Icarus 345, 113716. https://doi.org/10.1016/j.icarus.2020.113716.
Peplowski, P.N., 2016. Remote sensing evidence for an ancient carbon-bearing crust on Mercury. Nat. Geosci. 9, 273–276.
Peplowski, P.N., Stockstill-Cahill, K., 2019. Analytical identification and characterization of the major geochemical Terranes of Mercury's northern hemisphere. J. Geophys. Res. 124, 2414–2429.
Peplowski, P.N., Evans, L.G., Hauck, S.A., McCoy, T.J., Boynton, W.V., Gillis-Davis, J.J., Ebel, D.S., Goldsten, J.O., Hamara, D.K., Lawrence, D.J., McNutt, R.L., Nittler, L.R., Solomon, S.C., Rhodes, E.A., Sprague, A.L., Starr, R.D., Stockstill-Cahill, K.R., 2011. Radioactive elements on Mercury's surface from MESSENGER: implications for the planet's formation and evolution. Science 333 (6051), 1850–1852. https://doi.org/10.1126/science.1211576.
Peplowski, P.N., Lawrence, D.J., Feldman, W.C., Goldsten, J.O., Bazell, D., Evans, L.G., Head, J.W., Nittler, L.R., Solomon, S.C., Weider, S.Z., 2015. Geochemical terranes of Mercury's northern hemisphere as revealed by MESSENGER neutron measurements. Icarus 253, 346–363. https://doi.org/10.1016/j.icarus.2015.02.002.
Reitze, M.P., Weber, I., Morlok, A., Hiesinger, H., Bauch, K.E., Stojic, A.N., Helbert, J., 2020. Mid-infrared spectroscopy of crystalline plagioclase feldspar samples with various Al,Si order and implications for remote sensing of Mercury and other terrestrial Solar System objects. EPSL 554, 116697.
Reitze, M.P., Weber, I., Morlok, A., Hiesinger, H., Bauch, K.E., Stojic, A.N., Helbert, J., 2021. Mid-infrared spectroscopy of anorthosite samples from near manicouagan crater, Canada, as analogue for remote sensing of mercury and other terrestrial solar system objects. J. Geophys. Res. 126, e06832.
Renggli, C.J., Klemme, S., Morlok, A., Berndt, J., Weber, I., Hiesinger, H., King, P.L., 2022. Sulfides and hollows formed on Mercury's surface by reactions with reducing S-rich gases. Earth Planet. Sci. Lett. 593, 117647.
Rothery, D.A., Massironi, M., Alemanno, G., Barraud, O., Besse, S., Bott, N., Brunetto, R., Bunce, E., Byrne, P., Capaccioni, F., Capria, M.T., Carli, C., Charlier, B., Cornet, T., Cremonese, G., D'Amore, M., De Sanctis, M.C., Doressoundiram, A., Ferranti, L., Filacchione, G., Galluzzi, V., Giacomini, L., Grande, M., Guzzetta, L.G., Helbert, J., Heyner, D., Hiesinger, H., Hussmann, H., Hyodo, R., Kohout, T., Kozyrev, A., Litvak, M., Lucchetti, A., Malakhov, A., Malliband, C., Mancinelli, P., Martikainen, J., Martindale, A., Maturilli, A., Milillo, A., Mitrofanov, I., Mokrousov, M., Morlok, A., Muinonen, K., Namur, O., Owens, A., Nittler, L.R., Oliveira, J.S., Palumbo, P., Pajola, M., Pegg, D.L., Penttilä, A., Politi, R., Quarati, F., Re, C., Sanin, A., Schulz, R., Stangarone, C., Stojic, A., Tretiyakov, V., Väisänen, T., 2020. Rationale for bepicolombo studies of mercury's surface and composition. Space Sci. Rev. 216, 66.
Salisbury, J.W., 1993. Mid-infrared spectroscopy: laboratory data. In: Pieters, C.M., Englert, P.A.J. (Eds.), Remote Geochemical Analysis: Elemental and Mineralogical Composition. Cambridge University Press.
Salisbury, J.W., Wald, A., 1992. The role of volume scattering in reducing spectral contrast of reststrahlen bands in spectra of powdered minerals. Icarus 96, 121–123.
Salisbury, J.W., Walter, L.S., 1989. Thermal infrared (2.5–13.5 μm) spectroscopic remote sensing of igneous rock types on particulate planetary surfaces. J. Geophys. Res. 94, 9192–9202.
Salisbury, J.W., Walter, L.S., Vergo, N., D'Aria, D.M., 1991. Infrared (2,1–25 μm) Spectra of Minerals. Johns Hopkins University Press, Baltimore, MD.
Salisbury, J.W., Wald, A., Di Aria, D.M., 1994. Thermal-infrared remote sensing and Kirchhoff's law 1. Labaratory measurements. J. Geophys. Res. 99 (B6), 11897–11911.
Salisbury, J.W., Basu, A., Fischer, E.M., 1997. Thermal infrared spectra of lunar soils. Icarus 130, 125–139.
Sprague, A.L., Roush, T.L., 1998. Comparison of laboratory emission spectra with mercury telescopic data. Icarus 133, 174–183.
Sprague, A.L., Kozlowski, R.W.H., Wittebom, F.C., et al., 1994. Mercury: evidence for anorthosite and basalt from mid-infrared (7.5–13.5 micrometer) spectroscopy. Icarus 109, 156–167.
Sprague, A., Deutsch, L.K., Hora, J., Fazio, G.G., Ludwig, B., Emery, J., Hoffmann, W.F., 2000. Mid-infrared (8.1–12.5 μm) imaging of Mercury. Icarus 147, 421–432.
Sprague, A.L., Emery, J.P., Donaldson, K.L., Russell, R.W., Lynch, D.K., Mazuk, A.L., 2002. Mercury: mid-infrared (3–13.5 μm) observations show heterogeneous composition, presence of intermediate and basic soil types, and pyroxene. Meteorit. Planet. Sci. 37, 1255–1268.
Sprague, A., Warell, J., Cremonese, G., Langevin, Y., Helbert, J., Wurz, P., Veselovsky, I., Orsini, S., Milillo, A., 2007. Mercury's surface composition and character as measured by ground-based observations. Space Sci. Rev. 132, 399–431.
Sprague, A.L., Donaldson Hanna, K.L., Kozlowski, R.W.H., Helbert, J., Maturilli, A., Warell, J.B., Hora, J.L., 2009. Spectral emissivity measurements of Mercury's surface indicate Mg- and Ca-rich mineralogy, K-spar, Na-rich plagioclase, rutile, with possible perovskite, and garnet. Planet. Space Sci. 57, 364–383.
Stockstill-Cahill, K.R., McCoy, T.J., Nittler, L.R., Weider, S.Z., Hauck, S.A., 2012. Magnesium-rich crustal compositions on Mercury: Implications for magmatism from petrologic modeling. J. Geophys. Res. 117. CiteID E00L15.
Thomson, J.L., Salisbury, J.W., 1993. The mid-infrared reflectance of mineral mixtures (7–14 microns). Remote Sens. Environ. 45, 1–13.
Van der Meer, F., 1995. Estimating and simulating the degree of serpentinization of peridotites using hyperspectral remotely sensed imagery. Nonrenew. Res. 4, 84–98.
Vander Kaaden, K.E., McCubbin, F.M., 2016. The origin of boninites on Mercury: An experimental study of the northern volcanic plains lavas. Geochim. Cosmochim. Acta 173, 246–263.
Vander Kaaden, K.E., McCubbin, F.M., Nittler, L.R., Peplowski, P.N., Weider, S.Z., Frank, E.A., McCoy, T., 2017. Geochemistry, mineralogy, and petrology of Boninitic and Komatiitic rocks on the Mercurian surface: insights into the Mercurian mantle. Icarus. https://doi.org/10.1016/j.icarus.2016.11.041. in Press.
Vilas, F., 2016. Mineralogical indicators of Mercury's hollows composition in MESSENGER color observations. Geophys. Res. Lett. 43, 1450–1456.
Weber, I., Morlok, A., Bischoff, A., Hiesinger, H., Ward, D., Joy, K.H., Crowther, S.A., Jastrzebski, N.D., Gilmour, J.D., Clay, P.L., Wogelius, R.A., Greenwood, R.C., Franchi, I.A., Münker, C., 2016. Cosmochemical and spectroscopic properties of Northwest Africa 7325—A consortium study. Meteorit. Planet. Sci. 51, 3–30.
Weber, I., Morlok, A., Grund, T., Bauch, K.E., Hiesinger, H., Stojic, A., Joy, K.H., 2018. A mid-infrared reflectance database in preparation for space missions. In: Lunar and Planetary Science Conference, p. 1430.
Weber, I., Reitze, M.P., Heeger, M., Adolphs, T., Morlok, A., Stojic, A.N., Hiesinger, H., Arlinghaus, H.F., Helbert, J., 2021. The effect of excimer laser irradiation on mid-IR spectra of mineral mixtures for remote sensing. EPS 569, 117072.
Weider, S.Z., Nittler, L.R., Starr, R.D., Ellen, Crapster-Pregont, Peplowski, P.N., Denevi, B.W., Head, J.W., Byrne, P.K., Hauck, S.A., Ebel, D.S., Solomon, S.C., 2015. Evidence for geochemical terranes on mercury: global mapping of major elements with MESSENGER's X-ray spectrometer. Earth Planet. Sci. Lett. 416, 109–120.